Brazilian Journal of Physics
ISSN: 0103-9733
luizno.bjp@gmail.com
Sociedade Brasileira de Física
Brasil

Ojeda González, A.; Domingues, M. O.; Mendes, O.; Kaibara, M. K.; Prestes, A.
Grad-Shafranov Reconstruction: Overview and Improvement of the Numerical Solution Used in Space Physics
Brazilian Journal of Physics, vol. 45, núm. 5, 2015, pp. 493-509
Sociedade Brasileira de Física
São Paulo, Brasil

Braz J Phys (2015) 45:493–509
DOI 10.1007/s13538-015-0342-y

SOCIEDADE BRASILEIRA DE FÍSICA

GENERAL AND APPLIED PHYSICS

Grad-Shafranov Reconstruction: Overview and Improvement of the Numerical Solution Used in Space Physics

A. Ojeda González[1,3] · M. O. Domingues[2] · O. Mendes[3] · M. K. Kaibara[4] · A. Prestes[1]

Received: 12 September 2014 / Published online: 14 July 2015

Abstract The Grad-Shafranov equation is a Poisson's equation, i.e., a partial differential equation of elliptic type. The problem is depending on the initial condition and can be treated as a Cauchy problem. Although it is ill-posed or ill-conditioned, it can be integrated numerically. In the integration of the GS equation, singularities with large values of the potential arise after a certain number of integration steps away from the original data line, and a filter should be used. The Grad-Shafranov reconstruction (GSR) technique was developed from 1996 to 2000 for recovering two-dimensional structures in the magnetopause in an ideal MHD formulation. Other works have used the GSR techniques to study magnetic flux ropes in the solar wind and in the magnetotail from a single spacecraft dataset; posteriorly, it was extended to treat measurements from multiple satellites. From Vlasov equation, it is possible to arrive at the GS-equation in function of the normalized vector potential. A general solution is obtained using complex variable theory. A specific solution was chosen as benchmark case to solve numerically the GS equation. We propose some changes in the resolution scheme of the GS equation to improve the solution. The result of each method is compared with the solution proposed by Hau and Sonnerup (J. Geophys. Res. **104**(A4), 6899–6917 (1999)). The main improvement found in the GS resolution was the need to filter B_x values at each y value.

Keywords Grad-Shafranov equation · Magnetic flux-ropes · Cauchy problem · Space plasmas · Kinetic theory

✉ A. Ojeda González
ojeda.gonzalez.a@gmail.com

[1] Laboratory of Physics and Astronomy, IP&D, Universidade do Vale do Paraíba – UNIVAP, 12244-000 São José dos Campos, SP, Brazil

[2] LAC/CTE/National Institute for Space Research - INPE, 12227-010 São José dos Campos, SP, Brazil

[3] DGE/CEA/National Institute for Space Research - INPE, 12227-010 São José dos Campos, SP, Brazil

[4] GMA/IME/Fluminense Federal University-UFF, Rua Mário Santos Braga, s/n, Valonguinho, Centro, CEP 24020-140 Niterói, RJ, Brazil

1 Introduction

The pioneer studies about the Grad-Shafranov reconstruction (GSR) technique were developed from 1996 to 2000 [10, 14, 26] and have been applied to recovering two-dimensional (2-D) coherent magnetohydrostatic structures from spacecraft data (AMPTE/IRM and UKS) inside magnetopause.

Another candidate for application of the GSR was the magnetic flux-rope. The first paper written with this purpose has been published by [15]. A second paper was published by the same authors one year later [13]. The previous manuscripts are the core of the GSR of magnetic flux ropes in the solar wind (e.g., [22, 24]). Details of the reconstruction techniques employed by [13, 15] are the same described in [10]. Sonnerup et al. [28] proposed some modifications in the reconstruction method with the aim of extend to another

applications, which were discussed, but not included in the paper.

In addition, other works have used the GSR techniques to study magnetic flux ropes in the solar wind and in the magnetotail, using measurements from a single spacecraft [3, 12, 16, 20, 30, 31], and also extending the analysis to treat measurements from multiple satellites [7–9, 19, 21, 27, 29].

The limitations of the GSR method and its precision compared to other flux rope fitting techniques were studied by [1, 25]. The precision of GSR is affected when a spacecraft crosses the structure with a high impact parameter or when the structure is distorted [17]. For instance, improvements in construction of residual maps and numerical differentiation were studied by [17].

The aims of this paper are: first (revision), to group in a single paper physical and mathematical considerations used to obtain the GS equation, e.g., starting from the magnetostatic equilibrium equation ($\vec{\nabla} p = \vec{J} \times \vec{B}$), or using kinetic theory to obtain a specific form of the GS equation which has analytical solution; second (original contribution), to propose an improvement upon the numerical solution proposed by [10]. Also, here we show the equations used to calculate B_x, B_y, B_z, p, P_t, J_z, and resulting contour plots, which were not shown in previous works (only [19] showed some contour plots). In summary, Sections 1 and 2 are revision of earlier works; Sections 3, 4, and 5 are original contribution of this work.

1.1 Physical Consideration to Obtain the GS Equation

We present a summary of the theoretical concepts to obtain the GS equation (see physical-mathematical development of the Grad-Shafranov equation in Appendix):

1. 2.5-dimensional structures with $\hat{z}-$axis invariant, $\partial/\partial z = 0$ for any parameter.
2. The plasma gravity term is smaller than the magnetic term, and the plasma beta is small, $\beta \ll 1$ (in $\perp$ plane). The plasma beta is the ratio of the plasma pressure, $p = nk_BT$, to the magnetic pressure, $p_{mag} = B^2/2\mu_0$, where n is number density, k_B Boltzmann constant, T temperature, B magnetic field, and μ_0 magnetic permeability of the free space.
3. The gradient of the z-component of the vector potential ($\vec{\nabla} A_z$) is always $\perp$ to $\vec{B}$.
4. 2.5-D magnetic structure of a stationary plasma described by the balance of pressure force and magnetic forces ($\vec{J} \times \vec{B} = \vec{\nabla} p$), respectively, i.e., a magnetostatic equilibrium.
5. A stationary plasma means that the velocity of the particles is less than the Alfvén velocity, $v^2 \ll v_A^2$, ($v_A = B/(\sqrt{\mu_0 \rho})$, where ρ is the plasma density).
6. $\vec{\nabla} B_z \perp (\vec{J}_\perp$ and $\vec{B}_\perp)$.
7. $\vec{\nabla} A_z$ is in the $xy-$plane or $\perp$ plane, $\vec{\nabla} A_z \perp \hat{z}$.
8. p and A_z are constants along a magnetic field line.

The Grad-Shafranov equation is a Poisson's equation, i.e., a partial differential equation of elliptic type. The problem is depending on the initial condition and can be treated as a Cauchy problem, though it is ill-posed, and can be integrated numerically (e.g., [20]). The definition of ill-posed problems follows from the definition of well-posed problems given in 1923 by J. Hadamard (see [5]). He believed that mathematical models of physical phenomena should have the properties that, (1) a solution exists, (2) the solution is uniquely determined, and (3) the problem is stable on the spaces, i.e., the solution's behavior changes continuously with the initial conditions. The Dirichlet problem for Laplace's equation, and the heat equation with specified initial conditions, are two examples of well-posed problems. Ill-posed problems can be defined as problems for which at least one of the conditions above, which characterize well-posed problems, is violated. Therefore, the GS solution treated as a Cauchy problem is ill-posed because the third condition is violated.

The manuscript is divided in five sections. A theoretical revision using kinetic theory to obtain the GS equation and its analytical solution is presented in Section 2. In Section 3, the methodology is presented. Section 4 discusses some forms to solve numerically the GS equation. We are interested in improving the numerical solution. In Section 5, the conclusions are shown.

2 Revision of Earlier Works

Kinetic theory can be used to obtain some analytical solutions of GS equation, which will be explained at the first part of this section. The analytical solution $A(x, y)$ can be visualized in a rectangular grid. Other physical parameters, e.g., B, p, J_z, P_t and P_{Total}, will be studied in the second part of this section.

2.1 Theoretical Revision: Kinetic Theory to Obtain Exact Solution of GS Equation

The Boltzmann equation with collision term can be written as

$$\frac{\partial f_j(\vec{r}, \vec{v}, t)}{\partial t} + \vec{v} \cdot \vec{\nabla} f_j(\vec{r}, \vec{v}, t) + \vec{a} \cdot \vec{\nabla}_v f_j(\vec{r}, \vec{v}, t) = \left(\frac{\delta f_j}{\delta t}\right)_{coll}, \tag{1}$$

where $\vec{a} = \vec{F}/m_j$ is the particle acceleration and m_j its mass. f_j is the distribution function in phase space and is

defined as the density of representative points of j-type particles of phase space, at instant t, with coordinates $(\vec{r},\ \vec{v})$. The notation operators $\vec{\nabla}$ and $\vec{\nabla}_\upsilon$ are:

$$\vec{\nabla} = \hat{x}\frac{\partial}{\partial x} + \hat{y}\frac{\partial}{\partial y} + \hat{z}\frac{\partial}{\partial z} \tag{2}$$

$$\vec{\nabla}_\upsilon = \hat{x}\frac{\partial}{\partial \upsilon_x} + \hat{y}\frac{\partial}{\partial \upsilon_y} + \hat{z}\frac{\partial}{\partial \upsilon_z}. \tag{3}$$

The Vlasov equation is a partial differential equation that describes the time evolution of the distribution function in phase space and that directly incorporates the smoothed macroscopic internal electromagnetic fields [2]. It may be obtained from the Boltzmann equation (1) with the collision term $(\delta f_j/\delta t)_{coll}$ equal to zero, but including the internal smoothed fields in the force term,

$$\frac{\partial f_j}{\partial t} + \vec{\mathrm{v}}\cdot\vec{\nabla} f_j + \frac{1}{m_j}[\vec{F}_{ext} + q_j(\vec{E}_i + \vec{\mathrm{v}}\times\vec{B}_i)]\cdot\vec{\nabla}_\upsilon f_j = 0. \tag{4}$$

Here, $\vec{F}_{ext}$ represents the external force, including the Lorentz force associated with any externally applied electric and magnetic fields, and $\vec{E}_i$ and $\vec{B}_i$ are internal smoothed electric and magnetic fields due to the presence and motion of all charged particles inside the plasma. In order that the internal macroscopic electromagnetic fields $\vec{E}_i$ and $\vec{B}_i$ are consistent with the macroscopic charge and current densities existing in the plasma itself, they must satisfy Maxwell equations

$$\vec{\nabla}\cdot\vec{E}_i = \frac{\rho}{\epsilon_0} \tag{5}$$

$$\vec{\nabla}\cdot\vec{B}_i = 0 \tag{6}$$

$$\vec{\nabla}\times\vec{E}_i = -\frac{\partial\vec{B}_i}{\partial t} \tag{7}$$

$$\vec{\nabla}\times\vec{B}_i = \mu_0\left(\vec{J} + \epsilon_0\frac{\partial\vec{E}_i}{\partial t}\right) \tag{8}$$

with the plasma charge density ρ and the plasma current density $\vec{J}$ given by the expressions:

$$\rho(\vec{r},\ t) = \sum_j q_j n_j(\vec{r},\ t) = \sum_j q_j \int_\upsilon f_j(\vec{r},\ \vec{\mathrm{v}},\ t)d^3\upsilon \tag{9}$$

$$\vec{J}(\vec{r},\ t) = \sum_j q_j n_j(\vec{r},\ t)\vec{u}_j(\vec{r},\ t) = \sum_j q_j \int_\upsilon \vec{\mathrm{v}} f_j(\vec{r},\ \vec{\mathrm{v}},\ t)d^3\upsilon \tag{10}$$

the summations are over the different charged particle species in the plasma. Here, $\vec{u}_j(\vec{r},\ t)$ denote the macroscopic average velocity for the particles of type j. Equations (4) to (10) constitute a complete set of self-consistent equations to be solved simultaneously [2].

2.1.1 Formal Solution to Equilibrium Vlasov Equation

We may also arrive at the GS equation (66) using kinetic theory, and following the work of [33] an exact solution can be obtained. We will rewrite in this subsection a part of the work of [33], changing the magnetic field configuration. They used a 2D magnetic field configuration ($\vec{B}_i = B_{ix}(x,\ y)\hat{x} + B_{iy}(x,\ y)\hat{y}$). On the other hand, Sonnerup et al. [28] obtained the GS equation starting from balance of pressure forces and magnetic forces. They used a 2.5-D magnetic field configuration (see Appendix). However, those manuscripts have in common that both considered "Coulomb Gauge" ($\vec{\nabla}\cdot\vec{A}_i = 0$) and invariant axis ($\partial/\partial z = 0$), respectively. Both theories are equivalent when a 2.5-D magnetic structure is assumed ($\vec{B}_i = B_{ix}(x,\ y)\hat{x} + B_{iy}(x,\ y)\hat{y} + B_{iz}(x,\ y)\hat{z}$). The methodology presented by [33] is not affected when a 2.5-D magnetic structure (with $\partial/\partial z = 0$) is used.

A current sheet is confined to a surface which separates two regions of oppositely directed magnetic fields. For the investigation of a current sheet equilibrium, analytical methods and numerical simulations are used. The most extensively used model is the analytical Harris model, for which a distribution of electromagnetic fields is necessary. The aim is to study plasma confinement by magnetic fields. In this approximation, it is considered a particle system with ions and electrons that are represented by the gaussian functional form:

$$f_j(P_j, H_j) = N_j \exp\left((H_j - V_j P_j + m_j V_j^2/2)/T_j\right), \tag{11}$$

where species labeled $j = \{i,\ e\}$ correspond to ions and electrons, respectively. The multiplicative constants N_j, V_j, and T_j are related to the number density n_j, drift velocity and isotropic kinetic temperature. Therefore, the following conditions $\frac{\partial f_j}{\partial t} = 0$, $\vec{E}_i = 0$, and $\vec{F}_{ext} = 0$ are satisfied. The class of kinetic current sheet equilibrium to be discussed in the present subsection is a solution of the equilibrium Vlasov kinetic equation derived from the manuscript (4), (8), and (10):

$$[\vec{\mathrm{v}}\cdot\vec{\nabla} + (q_j/m_j)(\vec{\mathrm{v}}\times\vec{B}_i)\cdot(\partial/\partial\vec{\mathrm{v}})]f_j(\vec{r},\ \vec{\mathrm{v}}) = 0 \tag{12}$$

$$\vec{\nabla}\times\vec{B}_i = \mu_0\vec{J}, \tag{13}$$

In this configuration, the particle distribution depends on two spatial coordinates, $f_j = f_j(x,\ y,\ \vec{v})$. In (13), the left hand side of the Ampere's law is

$$\begin{aligned}\vec{\nabla}\times\vec{B}_i &= \vec{\nabla}\times\vec{\nabla}\times\vec{A}_i = \vec{\nabla}(\vec{\nabla}\cdot\vec{A}_i) - (\vec{\nabla}\cdot\vec{\nabla})\vec{A}_i \\ &= -\nabla^2\vec{A}_i = \mu_0\vec{J}. \end{aligned} \tag{14}$$

The problem is reduced to work with the z component of the above equation. In summary,

$$\begin{aligned}\nabla^2(A_{iz}(x,\ y)\hat{z}) &= \left(\frac{\partial^2 A_{iz}(x,\ y)}{\partial x^2} + \frac{\partial^2 A_{iz}(x,\ y)}{\partial y^2}\right)\hat{z} \\ &= -\mu_0 J_z(x,\ y)\hat{z}, \end{aligned} \tag{15}$$

and canonical momentum and the total Hamiltonian are:

$$P_j = m_j v_z + q_j A_{iz}(x, y), \quad H_j = m_j v^2/2. \tag{16}$$

Combining (11) and (16), gives

$$\begin{aligned}f_j(x,\ y,\ \vec{v}) &= N_j \exp\left(-\frac{m_j}{2T_j}[v_x^2 + v_y^2 + (v_z - V_j)^2 \right. \\ &\left. -\frac{2q_j V_j A_{iz}(x,\ y)}{m_j}]\right). \end{aligned} \tag{17}$$

Combining (10), (15), and (17) gives

$$\begin{aligned}\nabla^2 A_{iz} &= -\mu_0 \sum_j N_j q_j \exp\left(\frac{q_j V_j A_{iz}(x,\ y)}{T_j}\right) \\ &\times \int_{-\infty}^{\infty} \exp\left(-\frac{m_j v_x^2}{2T_j}\right) dv_x \\ &\times \int_{-\infty}^{\infty} \exp\left(-\frac{m_j v_y^2}{2T_j}\right) dv_y \\ &\times \int_{-\infty}^{\infty} v_z \exp\left(-\frac{m_j (v_z - V_j)^2}{2T_j}\right) dv_z, \end{aligned}$$

$$\begin{aligned}\nabla^2 A_{iz} &= -\mu_0 \sum_j N_j q_j \exp\left(\frac{q_j V_j A_{iz}(x,\ y)}{T_j}\right) \\ &\times \sqrt{\frac{2T_j\pi}{m_j}}\sqrt{\frac{2T_j\pi}{m_j}} \times \left(\int_{-\infty}^{\infty}(v_z - V_j)\right. \\ &\times \exp\left(-\frac{m_j (v_z - V_j)^2}{2T_j}\right) d(v_z - V_j) \\ &\left. + V_j \int_{-\infty}^{\infty} \exp\left(-\frac{m_j (v_z - V_j)^2}{2T_j}\right) d(v_z - V_j)\right), \end{aligned}$$

$$\begin{aligned}\nabla^2 A_{iz} &= -\mu_0 \sum_j N_j q_j \exp\left(\frac{q_j V_j A_{iz}(x,\ y)}{T_j}\right) \frac{2T_j\pi}{m_j} \\ &\left(0 + V_j\sqrt{\frac{2T_j\pi}{m_j}}\right), \end{aligned}$$

$$\begin{aligned}\nabla^2 A_{iz} &= -\mu_0 \sum_j q_j \pi^{3/2}\left(\frac{2T_j}{m_j}\right)^{3/2} \\ &\times N_j V_j \exp\left(\frac{q_j V_j A_{iz}(x,\ y)}{T_j}\right) \end{aligned}$$

$$\nabla^2 A_{iz} = -\mu_0 \sum_j q_j n_{0j} V_j \exp\left(\frac{q_j V_j A_{iz}}{T_j}\right) \tag{18}$$

where $n_j = n_{0j}\exp(q_j V_j A_{iz}(x,\ y)/T_j)$ is the number density, $v_{Tj}^2 = 2T_j/m_j$ is the thermal speed squared and $n_{0j} = \pi^{3/2} v_{Tj}^3 N_j$ is the maximum particle number density at the current sheet center [33].

An important plasma property is the stability of its macroscopic space charge neutrality. In this context, the expression to calculate plasma density is

$$\begin{aligned}\rho(x, y) &= \sum_j q_j n_j(x, y) \\ &= \sum_j q_j n_{0j} \exp(q_j V_j A_{iz}(x,\ y)/T_j) \\ &= -q_e n_{0e} \exp(-q_e V_e A_{iz}(x,\ y)/T_e) \\ &\quad + q_i n_{0i} \exp(q_i V_i A_{iz}(x,\ y)/T_i) \end{aligned} \tag{19}$$

The (19) becomes zero to $|q_e| = |q_i| = q$, $n_{0e} = n_{0i} = n_0$, and $V_i/T_i = -V_e/T_e$. We thus assume such a condition henceforth. Inserting the previous condition into (18) gives

$$\begin{aligned}\nabla^2 A_{iz} &= -\mu_0 q n_0 \left(\frac{V_i T_i}{T_i} - \frac{V_e T_e}{T_e}\right)\exp\left(\frac{qV_i}{T_i}A_{iz}\right) \\ &= -2\mu_0 n_0 (T_e + T_i)\frac{qV_i}{2T_i}\exp\left(\frac{qV_i}{T_i}A_{iz}\right) \end{aligned}$$

Yoon and Lui [33] have introduced two constants, $B_{i0}^2 = 2\mu_0 n_0(T_e + T_i)$, $L = 2T_i/(qB_{i0}V_i)$, where B_{i0} is the asymptotic magnetic field strength, and L is the characteristic scale length associated with the current sheet. The previous equation becomes

$$\nabla^2 A_{iz} = -\frac{B_{i0}}{L}\exp\left(\frac{qB_{i0}V_i}{2T_i}\frac{2A_{iz}}{B_{i0}}\right).$$

The normalized vector potential, $\Psi = -A_{iz}/(LB_{i0})$, is introduced.

$$\left(\frac{\partial^2}{\partial x^2} + \frac{\partial^2}{\partial y^2}\right)\left(L^2\frac{-A_{iz}}{LB_{i0}}\right) = \exp(-2\Psi).$$

$$\left(\frac{\partial^2}{\partial (x/L)^2} + \frac{\partial^2}{\partial (y/L)^2}\right)\Psi = \exp(-2\Psi). \tag{20}$$

Table 1 First row, the first three authors who have proposed specific solutions of (21). The expressions of the generating function is shown in the second row. The specific solutions are shown in the last row

Solutions:	Harris[a]	Fadeev[b]	Kan[c]
$g(\xi)=$	$\exp(\iota\xi)$	$f+\sqrt{1+f^2}\exp(\iota\xi)$	$\exp(\iota\xi-\frac{\iota b}{\xi})$
$\Psi=$	$\ln(\cosh Y)$	$\ln\left(f\cos X+\sqrt{1+f^2}\cosh Y\right)$	$\ln\frac{\cosh[Y(1+b/R^2)]}{\sqrt{(1+b/R^2)^2-4bY^2/R^4}}$[d]

[a] [6]
[b] [4]
[c] [18]
[d] $R^2=X^2+Y^2$

Then, introducing dimensionless variables, $X=x/L$, $Y=y/L$, the equilibrium Ampere's law, or Grad-Shafranov equation, becomes

$$\frac{\partial^2\Psi}{\partial X^2}+\frac{\partial^2\Psi}{\partial Y^2}=\exp(-2\Psi). \tag{21}$$

Thus, the problem of obtaining exact two-dimensional current sheet equilibrium solutions is summarized to solving the GS equation for $\Psi(X,\ Y)$.

The general solution in terms of complex variable, $\xi=X+\iota\ Y$, was obtained by [32]. He obtained the formal solution to (21) as follows:

$$\exp(-2\Psi)=\frac{4|g'|^2}{\left(1+|g|^2\right)^2}, \tag{22}$$

where $g'=dg(\xi)/d\xi$. There are infinite varieties of $g(\xi)$ in a purely mathematical sense, but not all choice will turn out to be useful from a physical perspective [33]. The first three proposals to solve the (21) using the Walker's method are shown in Table 1.

Previous solutions provide analytic expressions to study plasma confinement by magnetic fields and the existence of current sheets. The Harris solution is an exact one-dimensional solution in which the magnetic field varies in the z-direction and the current is in the y-direction [6]. Fadeev et al. [4] and [18] generalize the Harris solution to a two-dimensional situation.

2.2 Method: Benchmark Case

We are interested in solving the GS equation as a function of magnetic vector potential,

$$\nabla^2 A_z=-\mu_0\frac{d}{dA_z}\left(p+\frac{B_z^2}{2\mu_0}\right). \tag{23}$$

The above equation does not possess exact analytical solutions, perhaps could be solved by numerical means. In order to validate the numerical solution must be found an analytical solution to compare between them. Therefore, the equilibrium Vlasov kinetic equation using gaussian functional leads to the equilibrium Ampere's law in function of the normalized vector potential (see (21)).

If the (21) has a specific solution, then this solution satisfies the GS equation when the right side term is $\frac{-\mu_0 d}{dA_z}\left(p+\frac{B_z^2}{2\mu_0}\right)=\exp -2A_z$ (henceforth, $A_z=A$).

Finally, the Fadeed solution is selected to evaluate the numerical method. Fadeed solution is characterized by forming O-magnetic field lines or magnetic islands because between every pair of magnetic islands there is a magnetic null, or X point. This solution is selected because it coincides with the magnetohydrostatic islands observed inside the magnetopause by [10, 26].

Therefore, the GS equation, namely,

$$\nabla^2 A(\tilde{x},\tilde{y})=\exp(-2A(\tilde{x},\tilde{y})), \tag{24}$$

can be used [33]. If we choose $\tilde{x}$ and $\tilde{y}$ along the current sheet and to be perpendicular to the current sheet respectively, then the analytical solution is (see Table 1, column 3[1]):

$$A(\tilde{x},\tilde{y})=\ln\{\tilde{\alpha}\cos\tilde{x}+\sqrt{1+\tilde{\alpha}^2}\cosh\tilde{y}\}. \tag{25}$$

The pressure and B_z distributions chosen are: $p=\exp(-2A)/(3\mu_0)$, and $B_z=\exp(-A)/\sqrt{3}$. The parameter $\tilde{\alpha}$ describe a string of nonlinear magnetic islands separated by X-type neutral point [33]. The solution shown in (25) was derived of the Harris model [6] by [4] (Fadeev solution). A map of the exact solution $A(\tilde{x},\tilde{y})$ with $\tilde{\alpha}=0.225$ is shown in Fig. 1.

Figure 1 plots (25) in a grid of $\tilde{x}_{min}=0$ and $\tilde{x}_{max}=51$ with a total of 101 equidistant samples, separated by

[1] where $f=\tilde{\alpha}$, $X=\tilde{x}$, $Y=\tilde{y}$ and $\Psi=A(\tilde{x},\tilde{y})$

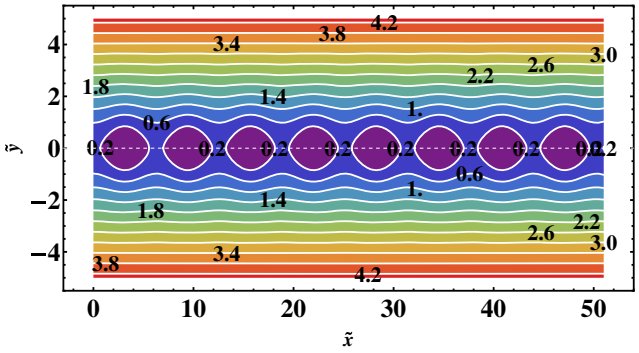

Fig. 1 Map of exact analytical solution (or benchmark solution). Field lines are separated by equal flux

$\Delta\tilde{x} = 51/101$, in the other axis $\Delta\tilde{y} = 0.1\Delta\tilde{x}$ with $\tilde{y}_{min} = -5$ and $\tilde{y}_{max} = 5$. The analytical solutions to $B_{\tilde{x}}, B_{\tilde{y}}, B_{\tilde{z}}$ are:

$$B_{\tilde{x}} = \frac{\partial A}{\partial \tilde{y}} = \frac{\sqrt{1+\tilde{\alpha}^2}\sinh\tilde{y}}{\tilde{\alpha}\cos\tilde{x} + \sqrt{1+\tilde{\alpha}^2}\cosh\tilde{y}}; \quad (26)$$

$$B_{\tilde{y}} = -\frac{\partial A}{\partial \tilde{x}} = \frac{\tilde{\alpha}\sin\tilde{x}}{\tilde{\alpha}\cos\tilde{x} + \sqrt{1+\tilde{\alpha}^2}\cosh\tilde{y}}; \quad (27)$$

$$B_{\tilde{z}} = \sqrt{\frac{\exp(-2A)}{3}} = \frac{1}{\sqrt{3}(\tilde{\alpha}\cos\tilde{x} + \sqrt{1+\tilde{\alpha}^2}\cosh\tilde{y})}. \quad (28)$$

In Fig. 2, a total of 51 equidistant measurements of each $B_{\tilde{x}}, B_{\tilde{y}}, B_{\tilde{z}}$ (left panel), $A(\tilde{x}, \tilde{y})$ (right panel) versus $\tilde{x}$ at $\tilde{y} = 0$ are plotted. The dataset were interpolated using cubic spline to obtain a total of 101 equidistant samples, separated by $\Delta\tilde{x}$, same as in [10].

We check the method to solve the GS equation using the benchmark case given by [10] and recalculated by [20]. We want to explain all the procedure in detail, i.e., here are shown some equations and graphs that do not appear in the earlier manuscripts.

For testing, a frame velocity $\vec{V}_{TH} - V_{HT} = 0.8\hat{\tilde{x}} + 0.08\hat{\tilde{y}} + 0.16\hat{\tilde{z}}$ onto the $\tilde{x}\tilde{y}$ plane was selected, as was proposed by [10]. The $\tilde{x}\tilde{y}$ coordinate system is rotated relative to the xy system by an angle of 5.7° ($\tan^{-1}(0.08/0.8) = 5.7°$). To rotate a figure counterclockwise around the origin by some angle, $\theta = 5.7^0$, is equivalent to replacing every point with coordinates $(\tilde{x},\ \tilde{y})$ by the point with coordinates $(x,\ y)$:

$$\tilde{x} = x\cos\theta - y\sin\theta$$
$$\tilde{y} = x\sin\theta + y\cos\theta.$$

Thus, the coordinates $(\tilde{x}\tilde{y})$ are changed by new coordinates xy in the exact solution, $A(\tilde{x}, \tilde{y})$:

$$A(x, y, \theta) = \ln\{\tilde{\alpha}\cos[\tilde{x}(x, y, \theta)] + \sqrt{1+\tilde{\alpha}^2}\cosh[\tilde{y}(x, y, \theta)]\}. \quad (29)$$

The map of the solution (29) is shown in Fig. 3a. We used a grid of $x_{min} = 0$ and $x_{max} = 51$ with a total of 101 equidistant samples, separated by $\Delta x = 51/101$, in the other axis $\Delta y = 0.1\Delta x$ with $y_{min} = -5$ and $y_{max} = 5$. Also, seven plasma parameters can be written in the xy coordinate system, i.e.,

$$B_x = \frac{\partial A}{\partial y} = \frac{\tilde{\alpha}\sin[\tilde{x}]\sin\theta + \sqrt{1+\tilde{\alpha}^2}\sinh[\tilde{y}]\cos\theta}{\tilde{\alpha}\cos[\tilde{x}] + \sqrt{1+\tilde{\alpha}^2}\cosh[\tilde{y}]}, \quad (30)$$

$$B_y = -\frac{\partial A}{\partial x} = \frac{\tilde{\alpha}\sin[\tilde{x}]\cos\theta - \sqrt{1+\tilde{\alpha}^2}\sinh[\tilde{y}]\sin\theta}{\tilde{\alpha}\cos[\tilde{x}] + \sqrt{1+\tilde{\alpha}^2}\cosh[\tilde{y}]}, \quad (31)$$

$$B_z = \sqrt{\frac{\exp(-2A(x, y))}{3}} = \frac{1}{\sqrt{3}(\tilde{\alpha}\cos[\tilde{x}] + \sqrt{1+\tilde{\alpha}^2}\cosh[\tilde{y}])}, \quad (32)$$

$$p = \frac{1}{3\mu_0(\tilde{\alpha}\cos[\tilde{x}] + \sqrt{1+\tilde{\alpha}^2}\cosh[\tilde{y}])^2}, \quad (33)$$

$$P_t = p + \frac{B_z^2}{2\mu_0} = \frac{1}{2\mu_0}\exp(-2A), \quad (34)$$

$$J_z = \frac{d(p + B_z^2/(2\mu_0))}{dA} = -\frac{1}{\mu_0}\exp(-2A), \quad (35)$$

$$P_{Total} = p + \frac{B^2}{2\mu_0} = \frac{1}{3\mu_0}\exp(-2A) + \frac{B_x^2 + B_y^2 + B_z^2}{2\mu_0}, \quad (36)$$

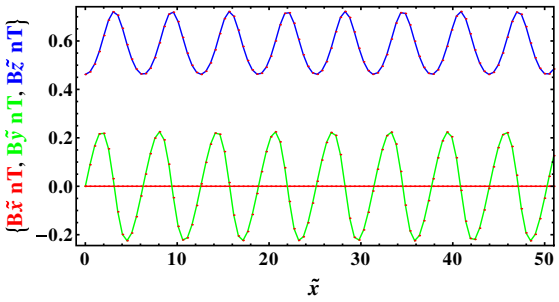

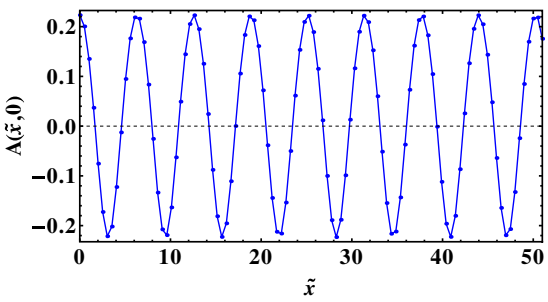

Fig. 2 Plot of $(B_{\tilde{x}}, B_{\tilde{y}}, B_{\tilde{z}},$ and $A(\tilde{x}, \tilde{y}))$ versus $\tilde{x}$ at $\tilde{y} = 0$

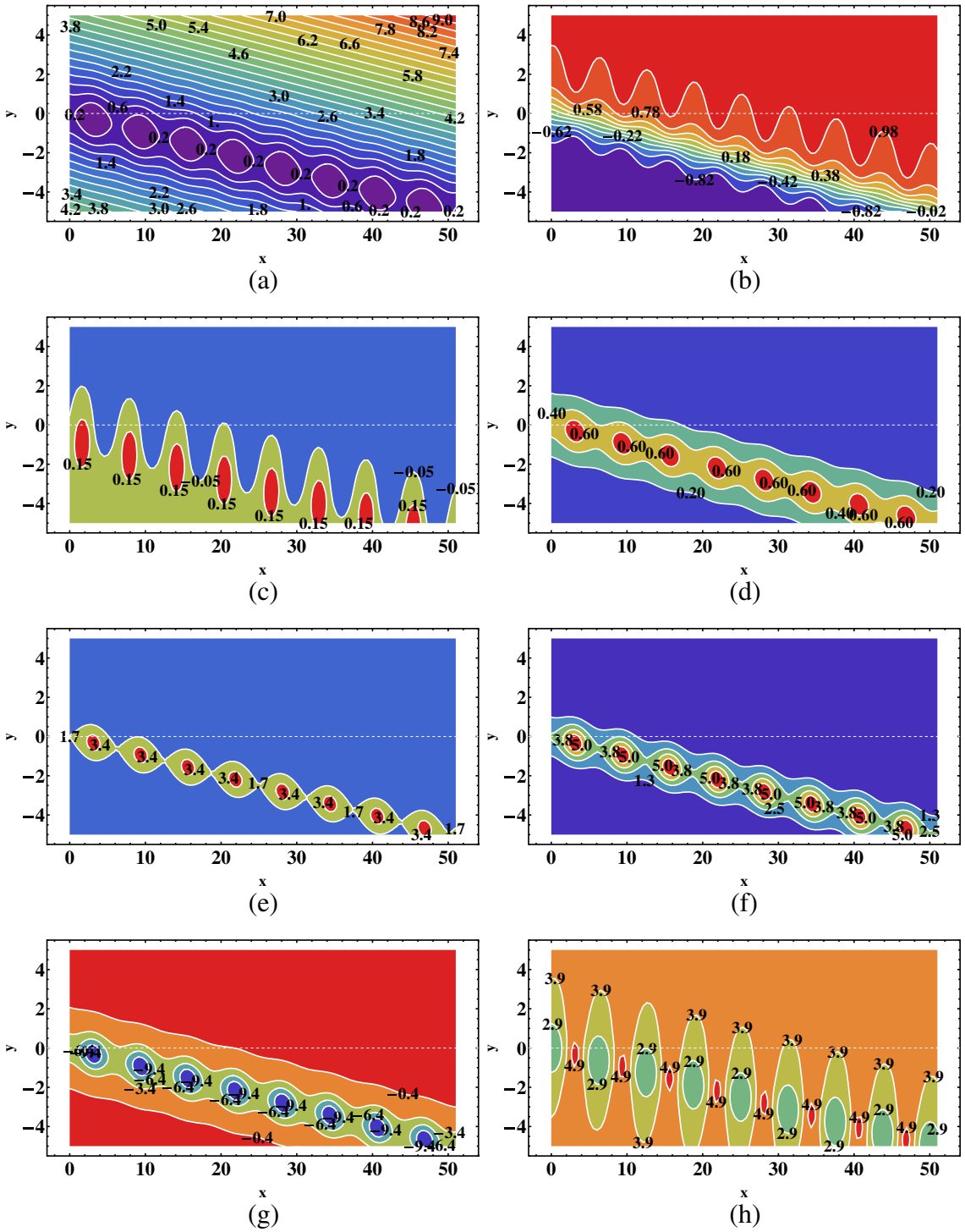

Fig. 3 (**a**) Map of exact analytical solution, $A(x, y)$ in xy plane. The $\tilde{x}\tilde{y}$ coordinate system is rotated relative to the xy system by an angle of 5.7°. Field lines are separated by equal flux. The other panels show the exact solution in xy plane of the other seven plasma parameters: (**b**) B_x; (**c**) B_y; (**d**) B_z; (**e**) p with normalization 10^5; (**f**) P_t with normalization 10^5; (**g**) J_z with normalization 10^5; (**h**) P_{Total} with normalization 10^5

where B_x, B_y, B_z are the magnetic field components; p is the plasma pressure; P_t is the transverse pressure; J_z is the axial current; P_{Total} is the total pressure; $\theta = 5.7°$; and the parameter $\tilde{\alpha} = 0.225$ is a separation constant that determines the properties of the solution. The term "transverse pressure" is used to define the pressure of plane transverse

to z axis, i.e, the pressure in the xy plane. In this context, the "transverse pressure" is anisotropic due to the field line curvature and it is not the same on different reference frames. However, the total pressure is always the same in any reference frame, any changes in B_z must be compensated for corresponding changes in B_x and B_y, respectively. Also, in this specific problem, the transverse pressure has a physical meaning when working with data sets measured by a spacecraft. It only makes physical meaning to solve the Grad-Shafranov equation in the deHoffmann-Teller (HT) frame [10].

The maps of previous equations, from (30) to (36), are shown in Fig. 3. Panel (a) is the map of exact analytical solution, $A(x, y)$ in xy plane. The other panels are the exact solution in xy plane of the other seven plasma parameters: (b) B_x; (c) B_y; (d) B_z; (e) p with normalization 10^5; (f) P_t with normalization 10^5; (g) J_z with normalization 10^5; (h) P_{Total} with normalization 10^5.

2.3 Numerical Solution

The numerical solution is useful to recover magnetic field maps that describe 2.5-dimensional, coherent field structures observed in magnetopause crossing by the spacecraft. The calculations required for the recovery consist of the numerical solution of the Grad-Shafranov equation, using as initial values magnetic field and plasma data collected by a single spacecraft along a straight-line trajectory, produced when structures are convected past it [10]. The focus of this manuscript is not to use data from the spacecraft to recover magnetic field maps. The aim is to work with the numerical solution using as initial values magnetic field and plasma data measured from the exact analytical solutions of Fadeed method. So, we can compare the exact analytical solution with the numerical solution to improve it.

We may write the second-order Taylor expansion [26] at the y values away from the "spacecraft trajectory" with step $\pm\Delta y$ in the integration process. The calculation starts at $y = 0$ (step 1):

$$A(x, \pm\Delta y) \cong A(x, 0) \pm \left(\frac{\partial A}{\partial y}\right)_{x,0} \Delta y + \\ + \frac{1}{2}\left(\frac{\partial^2 A}{\partial y^2}\right)_{x,0} (\Delta y)^2. \tag{37}$$

The function $A(x, \pm\Delta y)$ has been determined from the initial condition at points along the "spacecraft trajectory" with $y = 0$, i.e.:

$$A(x, 0) = -\int_0^x B_y(x'', 0)dx'' \\ (\partial A/\partial y)_{x,0} = B_x(x, 0).$$

Also, a single-valued function $P_t(A)$ is used to fit the spacecraft data along $y = 0$, i.e., $[d(p + B_z^2/2\mu_0)/dA]_{x,0}$. The second derivative in (37) can be evaluated from GS (66), as in [10]:

$$\left(\frac{\partial^2 A}{\partial y^2}\right)_{x,0} = -\left(\frac{\partial^2 A}{\partial x^2}\right)_{x,0} - \mu_0 \frac{dP_t(A(x, 0))}{dA}. \tag{38}$$

Using finite differences with central scheme, one grid point will be lost at each end of the data interval, resulting in the rhombus-shaped integration domain, as was showed by [26]. Hau and Sonnerup [10] extended the integration domain to a rectangular box to do a second-order Taylor expansion for forward and backward differentiation, respectively (see Appendix):

$$\left(\frac{\partial^2 A}{\partial x^2}\right)_i = \frac{2A_i - 5A_{i\pm1} + 4A_{i\pm2} - A_{i\pm3}}{(\Delta x)^2} + \\ + O(\Delta x^2) \text{ (forward(+) and backward(-))} \tag{39}$$

$$\left(\frac{\partial^2 A}{\partial x^2}\right)_i = \frac{A_{i+1} - 2A_i + A_{i-1}}{(\Delta x)^2} + \\ + O(\Delta x^2) \text{ (central).} \tag{40}$$

The plot of $P_t(A)$ vs A can be fit by a third order polynomial with exponential tails; differentiating it to put on the right-hand side of the GS (38). Thus, (38) is ready to put into (37) to calculate $A(x, \pm\Delta y)$ and start the new integration step.

However, a smoothing procedure is applied upon the solution of A, at each integration step, in order to reduce spurious results:

$$\bar{A}_1 = \omega(y)A_1 + \frac{1}{2}(1 - \omega(y))(A_1 + A_2), \\ \bar{A}_i = \omega(y)A_i + \frac{1}{2}(1 - \omega(y))(A_{i-1} + A_{i+1}) \text{ and} \\ \bar{A}_N = \omega(y)A_N + \frac{1}{2}(1 - \omega(y))(A_N + A_N), \tag{41}$$

where the subscript i denotes position along x. The weight $\omega(y)$ is a chosen function of y, i.e.,

$$\omega(y) = \begin{cases} 1 & \text{for } y = 0, \\ 1 - \frac{1}{3}\left|\frac{y}{y_{max}}\right| & \text{for other,} \\ 2/3 & \text{for } y = |y_{max}|. \end{cases} \tag{42}$$

This approach suppresses growth at short wavelengths but does not eliminate the development of singularities associated with the longer wavelengths [10].

The B_y values are found by $B_y(x, \pm\Delta y) = -(\partial A/\partial x)_{x,\pm\Delta y}$ using finite differences scheme (see Appendix):

$$(\partial A/\partial x)_i = (A_{i+1} - A_{i-1})/(2\Delta x) + O(\Delta x^2) \tag{43}$$

The B_x values are obtained from the first-order Taylor expansion to the next step of integration:

$$B_x(x, \pm\Delta y) \cong B_x(x, 0) \pm (\partial^2 A/\partial y^2)_{x,0}\Delta y,$$

where we require again the GS equation (38).

In step 2, $y = \pm\Delta y$,

$$A(x, \pm 2\Delta y) \cong A(x, \pm\Delta y) \pm \left(\frac{\partial A}{\partial y}\right)_{x,\pm\Delta y} \times\Delta y + \frac{1}{2}\left(\frac{\partial^2 A}{\partial y^2}\right)_{x,\pm\Delta y}(\Delta y)^2, \quad (44)$$

$$B_y(x, \pm 2\Delta y) \cong -(\partial A/\partial x)_{x\pm 2\Delta y}, \quad (45)$$

$$B_x(x, \pm 2\Delta y) \cong B_x(x, \pm\Delta y) \pm (\partial^2 A/\partial y^2)_{x,\pm\Delta y}\Delta y. \quad (46)$$

And at step n, where $y = \pm(n-1)\Delta y$:

$$A(x, \pm n\Delta y) \cong A(x, \pm(n-1)\Delta y) \pm \left(\frac{\partial A}{\partial y}\right)_{x,\pm(n-1)\Delta y} \times\Delta y + \frac{1}{2}\left(\frac{\partial^2 A}{\partial y^2}\right)_{x,\pm(n-1)\Delta y}(\Delta y)^2 \quad (47)$$

$$B_y(x, \pm n\Delta y) \cong -(\partial A/\partial x)_{x\pm n\Delta y}, \quad (48)$$

$$B_x(x, \pm n\Delta y) \cong B_x(x, \pm(n-1)\Delta y) \pm (\partial^2 A/\partial y^2)_{x,\pm(n-1)\Delta y}\Delta y. \quad (49)$$

The GS equation is solved as a spatial initial value problem. The map of the numerical solution, $A(x, y)$, can be determined from the initial condition at point $y = 0$. The plots of B_x, B_y, B_z at $y = 0$ as function of x are shown in Fig. 4a. Panel (b) shows the plot of A at $y = 0$ as function of x, while panel (c) represents the plot of the plasma pressure, $p(x, 0)$. Figure 4d shows the curve of measured values of $P_t(x, 0) = (p + B_z^2/2\mu_0)$ versus their corresponding $A(x, 0)$ values; the curve fitting is $P_t(x, 0) = 0.398\exp(-2A(x, 0))$.

The map of numerical solution of GS equation is shown in Fig. 5a. Figure 5 has the same format as Fig. 3 but it was obtained from the numerical solution of Grad-Shafranov equation. In all panels, the highest error observed is on the bottom right corner. The numerical solutions have been plotted with the improved resolution, which will be discussed in the next section.

3 Methodology

In the integration of the GS equation, singularities with large values of the potential arise after a certain number of integration steps away from the original data line [10]. In the integration scheme of the GS equation (66), the main problem is caused by the right hand term, dP_t/dA, because there is nonlinearity of the equation. The great

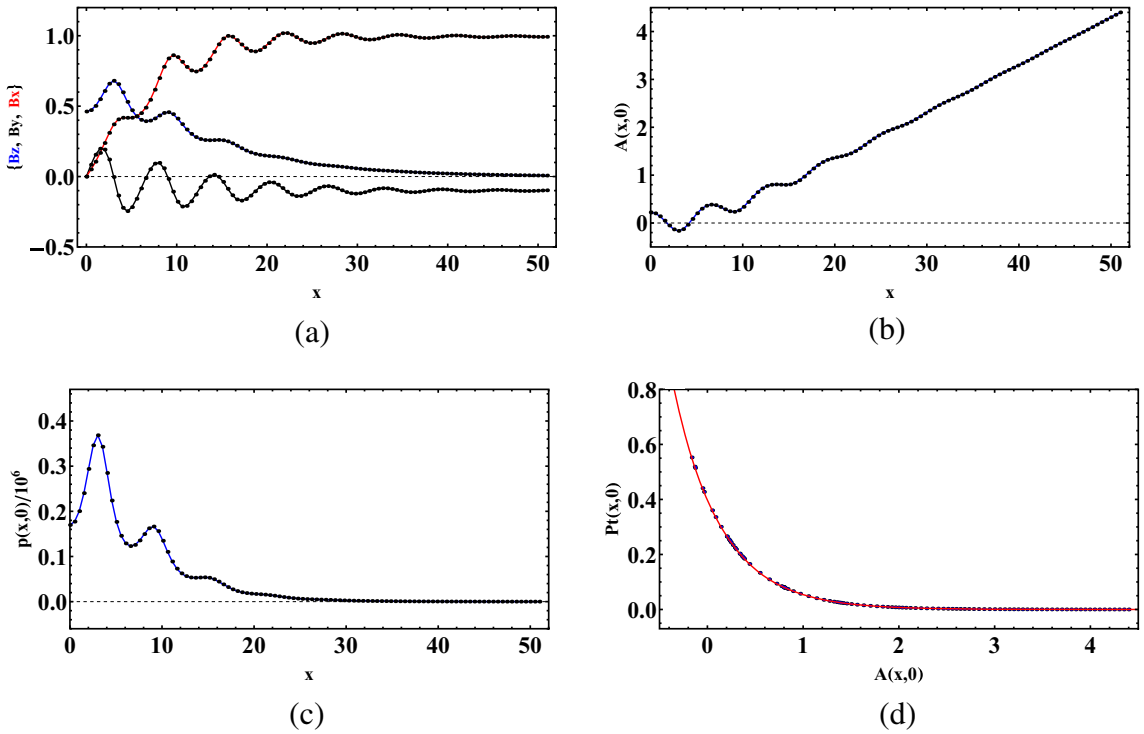

Fig. 4 Reconstruction of benchmark case with invariant (z) axis rotated around $\theta = 5.7°$. (**a**) B_x, B_y, B_z at $y = 0$ as function of x; (**b**) A at $y = 0$ as function of x; (**c**) p at $y = 0$ as function of x; and (**d**) P_t as function of A at $y = 0$, the curve fitting is $Pt(A) = 0.398\exp(-2A)$

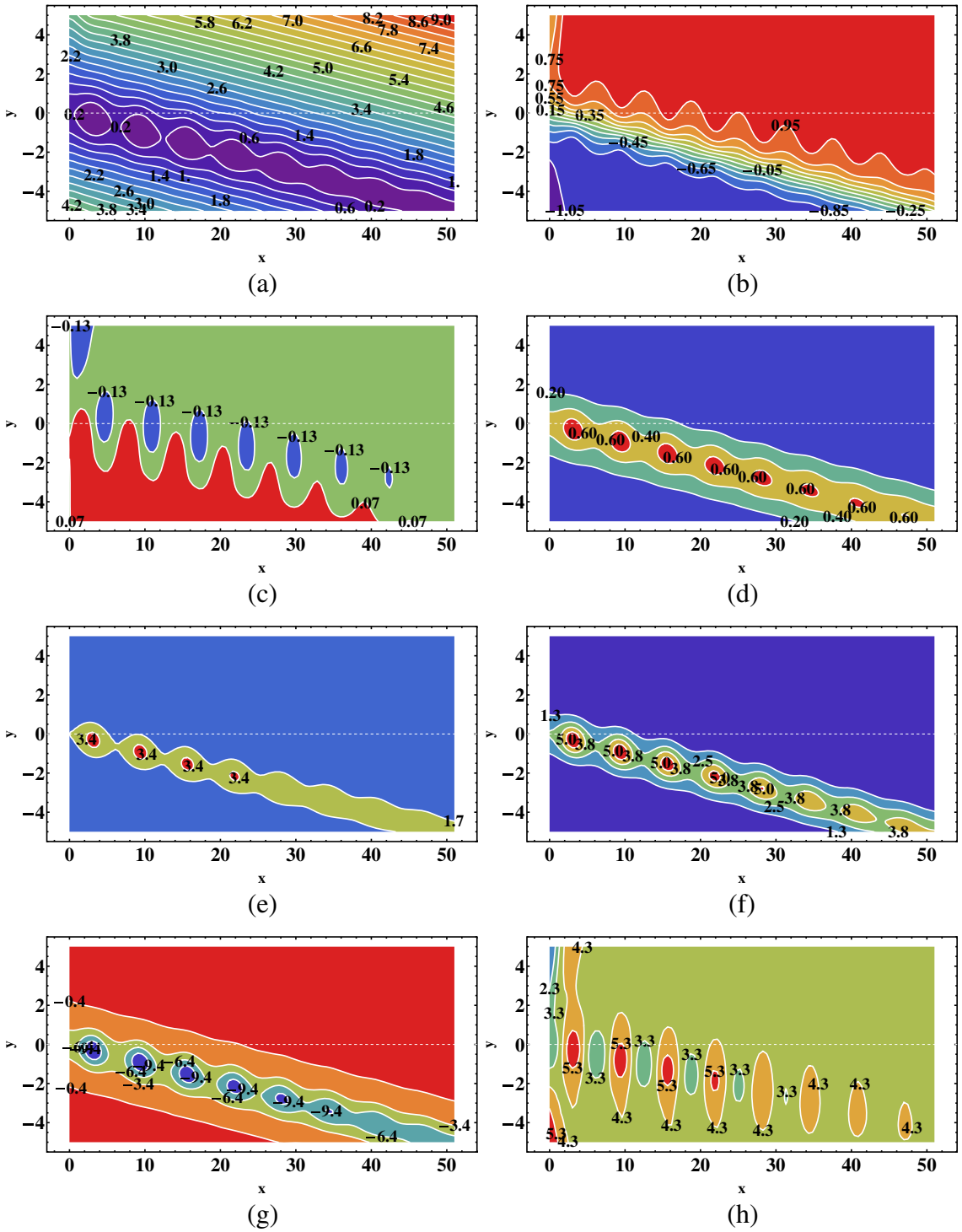

Fig. 5 (**a**) Map of numerical solution, $A(x, y)$ in xy plane. The $\tilde{x}\tilde{y}$ coordinate system is rotated relative to the xy system by an angle of 5.7°. Field lines are separated by equal flux. The other panels show the numerical solution in xy plane of the other seven plasma parameters: (**b**) B_x; (**c**) B_y; (**d**) B_z; (**e**) p with normalization 10^5; (**f**) P_t with normalization 10^5; (**g**) J_z with normalization 10^5; (**h**) P_{Total} with normalization 10^5

values of P_t could create singular points, to make a correct reconstruction. However, [17] reported that finite difference approximation used to estimate $\partial^2 A/\partial x^2$ is very unstable when dealing with noisy data. They used a filter (smooth noise-robust differentiators) development by [11] to suppress high-frequency noise. In this paper, we worked with signals obtained from an analytical solutions, and thought the noise should not be a problem. This section discusses

some forms to solve the GS equation using the same scheme, but with some modifications, proposed by [10].

The first step to improve the numerical solution of the GS equation is to obtain the same solution as [10, Fig.1]. The previous result will be useful to validate the proposed solution. Therefore, Fig. 6 is shown. In this figure, panel (a) is the same graphic shown in Fig. 3a, i.e., map of exact solution A(x,y); panel (b) is the numerical solution derived from the initial condition, as shown in Fig. 4. The integration domain was extended to 51 points in the x axis and from -5 to 5 in the y axis because in [10], the domain is $0 < x < 40$ and $-2.5 < y < 2.5$. Panel (c) shows the contours of constant error, $(A_{calc} - A_{exact})/\langle|A|\rangle$, where $\langle|A|\rangle$ is the average of the magnitude of A over the map. Panel (d) is a zoom of (c), so that it is equal to Figure 1 (bottom panel) of [10].

We propose some changes in the resolution scheme of the GS equation to improve the solution. We will be talking about four methods:

1. (HS99 method) The solution is the same that was explained in the paper of [10]. In that version, they attempt to suppress the development of the singularities associated with the shortest wavelengths by running a filter (see Eqs. 10 and 11 in that paper) in $A(x,\ \Delta y)$ for each integration step. The previous numerical solution map with its contours of constant error map is shown in the panels of Fig. 6. The more important information is that here, $B_x(x, \Delta y)$ is not filtered (see Fig. 7b), and in the difference scheme at each step, Δy second-order Taylor expansion with second order of accuracy was used.
2. (first method) At step n, where $y = \pm(n-1)\Delta y$; firstly, $A(x, \pm(n-1)\Delta y)$ and $B_x(x, \pm(n-1)\Delta y)$ are filtered respectively with HS99 filter; secondly, $A(x, \pm(n)\Delta y)$ is calculated using (47) and the finite difference scheme shown in Appendix is used to calculate $(\partial^2 A/\partial x^2)_i$.
3. (second method) At step n, $B_x(x, \pm(n-1)\Delta y)$ is not filtered while $A(x, \pm(n-1)\Delta y)$ is filtered. $A(x, \pm(n)\Delta y)$ is calculated using (47). The derivative $(\partial^2 A/\partial x^2)_i$ is calculated numerically, using a central difference scheme at each step Δy of the integration, resulting in the rectangular box by writing it at the i point, a second-order Taylor expansion with sixth order of accuracy (see that above was used second order accuracy): $(\partial^2 A/\partial x^2)_i = (\frac{1}{90}A_{i-3} - \frac{3}{30}A_{i-2} + \frac{3}{2}A_{i-1} - \frac{49}{18}A_i + \frac{3}{2}A_{i+1} - \frac{3}{20}A_{i+2} + \frac{1}{90}A_{i+3})/(\Delta x)^2 + O(\Delta x^2)$.
4. (third method) It is a combination of the first method and second method, respectively.

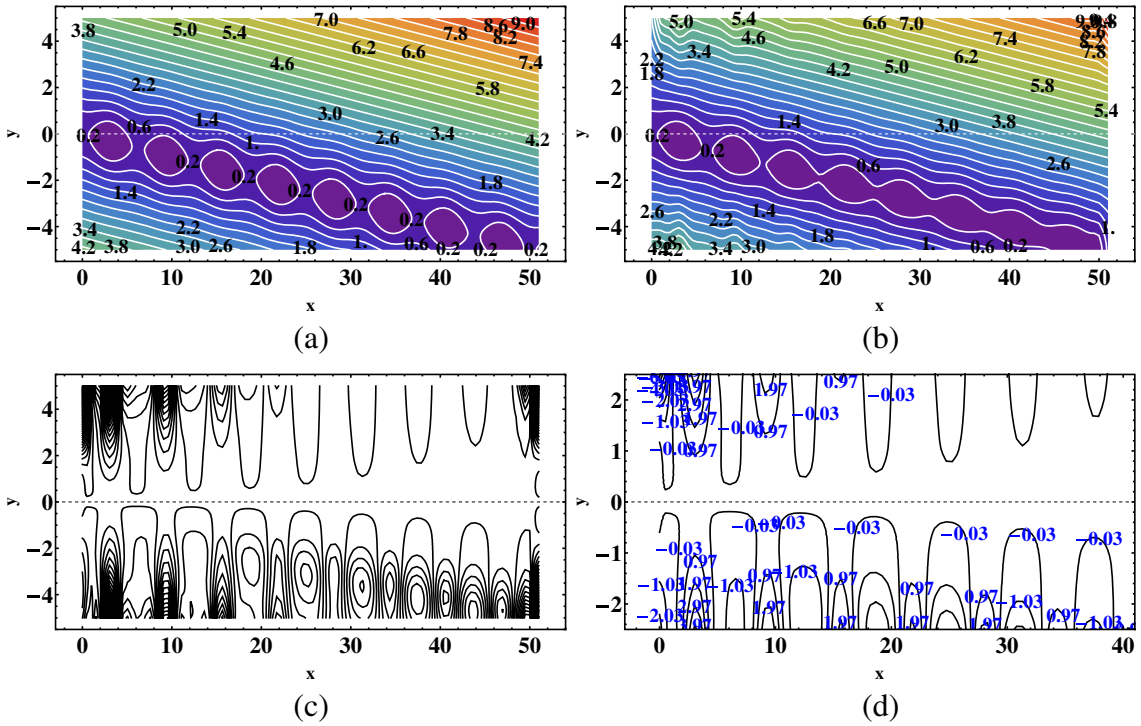

Fig. 6 Contours of constant error, $(A_{calc} - A_{exact})/\langle|A|\rangle$, where $\langle|A|\rangle$ is the average of the magnitude of A over the map. Error contours are separated by 1 %. (**a**) Analytical solution map of $A(x, y)$; (**b**) numerical solution map of $A(x, y)$; (**c**) contours of constant error; (**d**) zoom of contours of constant error, idem shown in Figure 1 of [10]

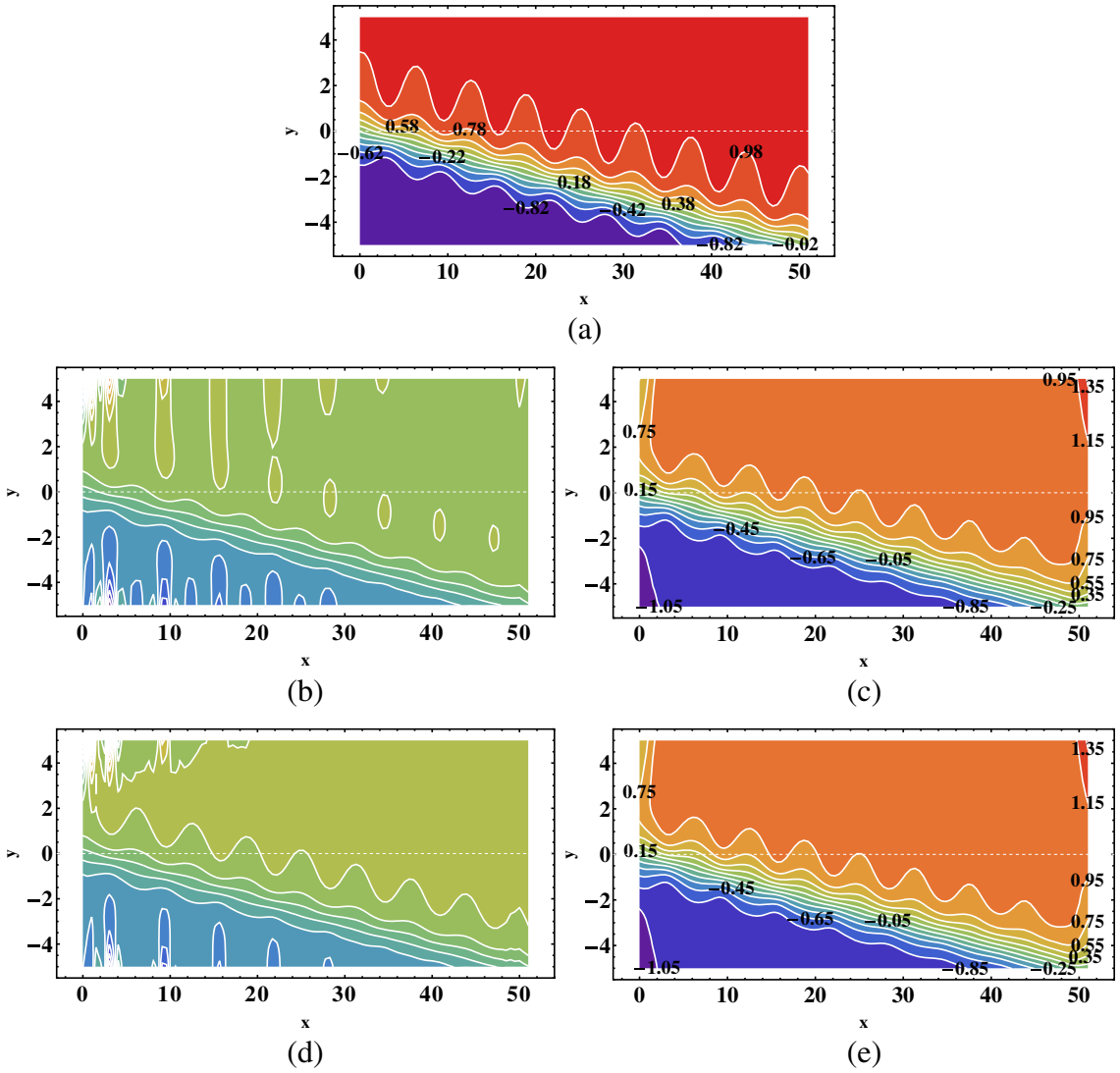

Fig. 7 (**a**) Map of exact analytical solution, $B_x(x, y)$ in xy plane. The other panels show numerical solution maps of B_x, where the following methods are used: (**b**) HS method, (**c**) first method, (**d**) second method, and **e** third method

4 Results and Discussion

Figure 7a shows the exact solution map of B_x. The panels (b) and (d) show numerical solution map of B_x without filtering; in both panels "HS99 method" and "second method" are used, respectively. Panel (c) shows map of B_x using the first method (B_x is filtered), and the numerical solution has been improved. In panel (e), the third method is used, and it improved the numerical solution. Grad-Shafranov equation has the nonlinearity in the term $d(P_t)/dA$; during the integration scheme, B_x values are obtained from the first order Taylor expansion,

$$B_x(x, \pm\Delta y) \cong B_x(x, 0) \pm (\partial^2 A/\partial y^2)_{x,0}\Delta y, \tag{50}$$

and the second derivative in the previous equation can be evaluated from GS equation,

$$\left(\frac{\partial^2 A}{\partial y^2}\right)_{x,0} = -\left(\frac{\partial^2 A}{\partial x^2}\right)_{x,0} - \mu_0 \frac{dP_t(A(x,0))}{dA}. \tag{51}$$

This justifies the need of filtering B_x during the integration scheme.

After obtaining the solution, the integration domain is reduced to remove the influence of the boundaries. Thus, in Fig. 8, the maps of $A(x, y)$ are shown in a grid of $5 \lesssim x \lesssim 45$ and $-4.5 \lesssim y \lesssim 4.5$. Each pair of panels from top to bottom show (a) the exact solution map and (b) contours of constant error, $(A_{calc} - A_{exact})/\langle|A|\rangle$, using the HS99

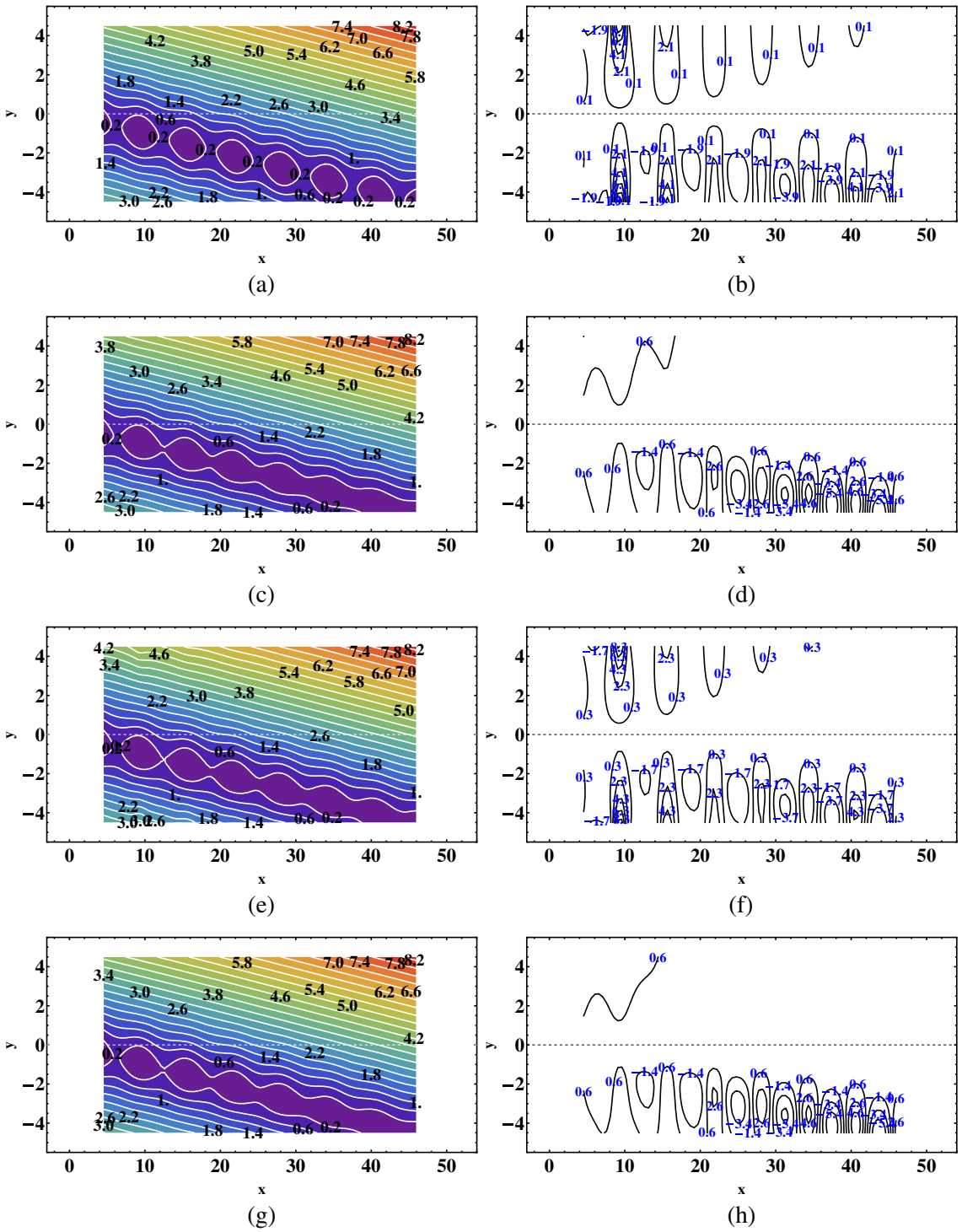

Fig. 8 Each pair of panels from top to bottom show: (**a**) the exact solution map and (**b**) contours of constant error, $(A_{calc} - A_{exact})/\langle|A|\rangle$, using the HS99 method; (**c**, **d**) the numerical solution map using the first method and contours of constant error; (**e**, **f**) are similar to (**c, d**) but for the second method; (**g, h**) are similar to (**c, d**) but for the third method

method; (c) and (d) the numerical solution map using the first method and contours of constant error; (e) and (f) have the same format that (c) and (d), but the second method is used; (g) and (h) have the same format that (c) and (d), but the third method is used.

In Fig. 8, panels of contours of constant error (d, f, and g) are compared with panel (b). The solution greatly improves when the first method is used (see panel (d)). In particular, the solution is not improved when using the second method (see panel (f)). The third method also improves the solution

and is the best method (see panel (h)). In summary, the solution in the paper of [10] was improved with these proposals. Other method to improve the GS solver is presented by the authors [16, Appendix A].

The contribution proposed here is important because if another filter is used, then need to use the methodology we are proposing, i.e., during the integration scheme also B_x should be filtered. It is a fact that our approach, when compared with HS99 method, reduces the errors at upper part of $A(x, y)$ contour plot. We found, in this context, that in two manuscripts [16, 17], the numerical solutions of the GS equation have been improved, but they did not propose filter B_x.

5 Conclusion

The Vlasov equation is a partial differential equation that describes the time evolution of the distribution function in phase space. It may be obtained from the Boltzmann equation with the collision term $(\delta f_j/\delta t)_{coll}$ equal to zero, but including the internal smoothed fields in the force term. The solution to equilibrium Vlasov equation may be constructed of infinitely many possible choices. The gaussian functional form $(f_j(P_j,\ H_j))$, from [6], was selected. This is a function of the canonical momentum (P_j) and the total Hamiltonian (H_j). The solution of $f_j(P_j,\ H_j)$ will satisfy the current and charge neutrality only if $n_{0e} = n_{0i} = n_0$ and $V_i/T_i = -V_e/T_e$.

The distribution function f_j (with $\partial/\partial z = 0$) is inserted into the equilibrium Vlasov kinetic equation. Then, the equilibrium Ampere's law is obtained (see 18). Some constants are introduced: B_0^2, X, Y, Ψ, and L, where Ψ is the normalized vector potential. The GS equation is obtained in function of it.

The general solution $\Psi(X, Y)$ in terms of complex variable, $\xi = X + \imath Y$, has the form $\Psi = (-1/2)\ln[4|g'|^2)/(1+|g|^2)^2]$ where $g' = dg(\xi)/d\xi$. The previous is known as the Walker's solution. The problem is reduced in obtaining the form of the generating function $g(\xi)$. There are infinite varieties of $g(\xi)$ in a purely mathematical sense, but not all choices will turn out to be useful from a physical perspective. The Harris's model solution is $\Psi = \ln(\cosh Y)$. The Fadeev's model solution is $\Psi = \ln(f\cos X + \sqrt{1+f^2}\cosh Y)$.

We choose $f = \tilde{\alpha}$, $X = \tilde{x}$, $Y = \tilde{y}$, and $\Psi = A(\tilde{x},\ \tilde{y})$, then the GS equation is transformed into $\nabla^2 A(\tilde{x},\ \tilde{y}) = \exp(-2A(\tilde{x},\ \tilde{y}))$ and the analytical solution is $A(\tilde{x},\ \tilde{y}) = \ln(\tilde{\alpha}\cos\tilde{x} + \sqrt{1+\tilde{\alpha}^2}\cosh\tilde{y})$. The previous solution was used as benchmark case to improve the numerical solution.

For testing, a frame velocity $\vec{V}_{TH} - V_{HT} = 0.8\hat{\tilde{x}} + 0.08\hat{\tilde{y}} + 0.16\hat{\tilde{z}}$ onto the $\tilde{x}\tilde{y}$ plane was selected, as was proposed by [10]. The $\tilde{x}\tilde{y}$ coordinate system is rotated relative to the xy system by an angle of 5.7°. The exact solutions for the other physical parameters, i.e., B_x, B_y, B_z, p, P_t, J_z, and P_{Total} are obtained.

The GS equation is a Poisson's equation, i.e., a partial differential equation of elliptic type. The problem depends on the initial condition and can be treated as a Cauchy problem, although it is ill-posed or ill-conditioned, and can be integrated numerically. We may write the second-order Taylor expansion at the y values away from the virtual spacecraft trajectory with step $\pm\Delta y$ in the integration process. The map of the numerical solution, $A(x,\ y)$, can be determined from the initial condition at point $y = 0$, i.e., $A(x,\ 0) = -\int_0^x B_y(x'',\ 0)dx''$, $B_x(x,\ 0)$, $p(x,\ 0)$, and $[d(p + B_z^2/2\mu_0)/dA]_{x,\,0}$.

In the integration of the GS equation, singularities with large values of the potential arise after a certain number of integration steps away from the original data line. In the integration scheme, the development of the singularities associated with the shortest wavelengths may be suppressed, and a filter should be used about A values at each y value. In the integration scheme of the GS equation, the main problem is caused by the right hand term, dP_t/dA, because there is the nonlinearity of the equation.

We proposed three modifications in the method to solve numerically the GS-equation. The result of each method is compared with the solution proposed by [10]. The main improvement found in the GS resolution was the need to filter B_x values at each y value. This paper is a review of the proposed methodology by [10] and clarifies some aspects that were not explained by the authors. Note that other authors proposed to improve filter precision [16, 17]; however, these methods are not discussed here.

Acknowledgments This work was supported by grants from CNPq (grants 483226/2011-4, 301441/2013-8), FAPESP (grant 2012/072812-2), and CAPES (grant 1236-83/2012). A. Ojeda González thanks CAPES and CNPq (grant 141549/2010-6) for his PhD scholarship and CNPq (grants 150595/2013-1, 503790/2012-5) for his postdoctoral research support. We also wish to thank the anonymous referees.

Appendix

Physical-Mathematical Development of the Grad-Shafranov Equation

In the MHD theory, in 2.5-dimensional and stationary structures, the Lorentz force has to be balanced by a pressure force. It is known as magnetostatic equilibrium:

$$\vec{\nabla} p = \vec{J} \times \vec{B}, \tag{52}$$

where $\vec{J}$ is the current density and p the plasma pressure. We will solve this equation in a 2.5-D Cartesian Coordinate System where $z-$axis is invariant ($\partial/\partial z = 0$ for any physical quantity). Hereafter, vectors in xy plane are denoted by $\perp$, and (52) is given by

$$\begin{aligned}\frac{\partial p}{\partial x}\hat{x} + \frac{\partial p}{\partial y}\hat{y} + 0\hat{z} &= \left(\vec{J}_\perp + J_z\hat{z}\right) \times \left(\vec{B}_\perp + B_z\hat{z}\right),\\ \frac{\partial p}{\partial x}\hat{x} + \frac{\partial p}{\partial y}\hat{y} &= J_z\left(\hat{z} \times \vec{B}_\perp\right) + \left(\vec{J}_\perp \times \hat{z}\right) B_z\\ &\quad + J_z B_z\left(\hat{z} \times \hat{z}\right) + \vec{J}_\perp \times \vec{B}_\perp.\end{aligned}$$

In right-hand side, the first and second terms are into xy (or $\perp$) plane, the third term is zero, and the fourth term is a vector parallel to z-axis. However, the z- component of the left-hand side is zero, then the z-component of the right-hand side must also be zero, therefore $\vec{J}_\perp \times \vec{B}_\perp \equiv 0$, this is $\vec{J}_\perp \| \vec{B}_\perp$. This causes the system to be force-free magnetic field (e.g., [23]) out of the $xy-$plane, but the system is not completely force-free magnetic field itself, there is a force in the $xy-$plane to ensure the equilibrium. The (52) can be written as

$$\vec{\nabla} p = \vec{J} \times \vec{B} = J_z\left(\hat{z} \times \vec{B}_\perp\right) + \left(\vec{J}_\perp \times \hat{z}\right) B_z. \tag{53}$$

The expressions for $J_z\hat{z}$ and $\vec{J}_\perp$ are searched using Ampere's law, as

$$\vec{\nabla} \times \vec{B} = \mu_0 \vec{J} = \mu_0\left(\vec{J}_\perp + J_z\hat{z}\right). \tag{54}$$

Hereafter, to simplify calculations, the magnetic field will be written as a function of vector potential $\vec{A}$. Due to the fact that $\vec{\nabla} \cdot \vec{B} = 0$, $\vec{B}$ can always be written as the curl of a vector, therefore $\vec{B} = \vec{\nabla} \times \vec{A}$. This is because $\vec{\nabla} \cdot (\vec{\nabla} \times \vec{A}) = 0$. It is true that $\vec{A}$ is not unique, one may have to choose a gauge. But in any case, the definition $\vec{B} = \vec{\nabla} \times \vec{A}$ holds true with the assumption that the invariant direction is the z-direction, and $\partial/\partial z = 0$. This actually means the choice of a gauge, the so-called "Coulomb gauge" ($\vec{\nabla} \cdot \vec{A} = 0$). In this problem, $A_z(x,\ y)$ is used, the z-component of the vector potential $\vec{A}$. And the magnetic field vector should be written as

$$\vec{B} = \vec{\nabla} \times (A_z(x,\ y)\hat{z}) + B_z\hat{z} \text{ or} \tag{55}$$

$$\vec{B} = \left(\frac{\partial A_z(x,\ y)}{\partial y}; -\frac{\partial A_z(x,\ y)}{\partial x}; B_z(x,\ y)\right). \tag{56}$$

$A_z(x,\ y)$ is directly related to the magnetic flux in the xy-plane. The field lines in that plane are represented by $A_z(x,\ y) = const$ [28].

We also have

$$\begin{aligned}\vec{B} \cdot \vec{\nabla} A_z(x,\ y) &= \vec{\nabla} \times (A_z\hat{z}) \cdot \vec{\nabla} A_z\\ &\quad + B_z\hat{z} \cdot \vec{\nabla} A_z = 0 \text{ and} \qquad (57)\\ \vec{B} \cdot \vec{\nabla} p &= 0. \qquad (58)\end{aligned}$$

The previous equations implies that A_z (henceforth, $A_z = A$) and p are constants along field lines.

The curl of $\vec{B}$ is

$$\begin{aligned}\vec{\nabla} \times \vec{B} &= \vec{\nabla} \times (\vec{\nabla} \times (A\hat{z})) + \vec{\nabla} \times (B_z\hat{z}) \qquad (59)\\ &= -\nabla^2 A\hat{z} + \vec{\nabla}[\underbrace{\vec{\nabla} \cdot (A\hat{z})}_{=0}] + \vec{\nabla} B_z \times \hat{z} \qquad (60)\end{aligned}$$

Considering the (54) and (60),

$$\vec{J}_\perp + J_z\hat{z} = \frac{1}{\mu_0}\vec{\nabla} B_z \times \hat{z} - \frac{\nabla^2 A}{\mu_0}\hat{z},$$

where

$$\vec{J}_\perp = \frac{1}{\mu_0}\vec{\nabla} B_z \times \hat{z}, \tag{61}$$

and

$$\vec{J}_z = -\frac{\nabla^2 A}{\mu_0}\hat{z}. \tag{62}$$

If the vectors $\vec{J}_\perp$ and $\vec{B}_\perp$ are parallel, as indicated in the preceding paragraphs, then the vector $\vec{\nabla} B_z$ is perpendicular to $\vec{J}_\perp$ and $\vec{B}_\perp$, respectively. We recall that $\vec{\nabla} A$ is in the xy plane, i.e., $\vec{\nabla} A \perp \hat{z}$. With the following vector identity $\vec{C} \times (\vec{D} \times \vec{E}) = \vec{D}(\vec{E} \cdot \vec{C}) - \vec{E}(\vec{D} \cdot \vec{C})$ and using the equation $\vec{E}_\perp = \vec{\nabla} D \times \hat{z}$, we have that:

$$\begin{aligned}\hat{z} \times \vec{B}_\perp &= \hat{z} \times (\vec{\nabla} A \times \hat{z})\\ &= \vec{\nabla} A(\hat{z} \cdot \hat{z}) - \hat{z}(\vec{\nabla} A \cdot \hat{z})\\ &= \vec{\nabla} A, \qquad (63)\end{aligned}$$

because $\vec{\nabla} A \perp \hat{z}$, then $\hat{z} \times \vec{B}_\perp$ is a vector in $xy-$plane.

We use the (61) and the vector identity $(\vec{D} \times \vec{E}) \times \vec{C} = \vec{E}(\vec{D} \cdot \vec{C}) - \vec{D}(\vec{E} \cdot \vec{C})$ to obtain the following result:

$$\begin{aligned}\vec{J}_\perp \times \hat{z} B_z &= \frac{1}{\mu_0}(\vec{\nabla} B_z \times \hat{z}) \times \hat{z} B_z\\ &= \frac{B_z}{\mu_0}\left[\hat{z}(\vec{\nabla} B_z \cdot \hat{z}) - \vec{\nabla} B_z(\hat{z} \cdot \hat{z})\right]\\ &= -\frac{B_z}{\mu_0}\vec{\nabla} B_z. \qquad (64)\end{aligned}$$

Here, it was considered that $\vec{\nabla} B_z \perp \hat{z}$. Equation (64) represents a vector in the $xy-$plane. We make the substitution of the (62), (63), and (64) into (53):

$$\vec{J} \times \vec{B} = \vec{\nabla} p = -\frac{1}{\mu_0}\{[\nabla^2 A]\vec{\nabla} A + B_z\vec{\nabla} B_z\}. \tag{65}$$

As the vectors $\vec{\nabla} A$ and $\vec{\nabla} B_z$ are in $xy-$plane, then the (65) represents a vector in the same plane. Since p and $\vec{\nabla} B_z$ are constant along a field line and should be only functions of A, the following expressions must hold

$$\begin{aligned}\vec{\nabla} p &= (dp/dA)\vec{\nabla} A \text{ and}\\ \vec{\nabla} B_z &= (dB_z/dA)\vec{\nabla} A.\end{aligned}$$

Substituting into (65),

$$\frac{dp}{dA}\vec{\nabla}A = -\frac{1}{\mu_0}\{[\nabla^2 A]\vec{\nabla}A + B_z\frac{dB_z}{dA}\vec{\nabla}A\},$$

multiplied by $\cdot\frac{1}{\vec{\nabla}A}$, and solve to $\nabla^2 A$ in the previous equation

$$\frac{\nabla^2 A}{\mu_0} = -\frac{dp}{dA} - \frac{1}{2\mu_0}\frac{dB_z^2}{dA}.$$

Finally,

$$\begin{aligned}\nabla^2 A &= -\mu_0\frac{d}{dA}\left(p + \frac{B_z^2}{2\mu_0}\right) \\ &= -\mu_0 J_z.\end{aligned} \tag{66}$$

The (66) is known as Grad-Shafranov equation; note that (24, where the right-hand side is an exponential), is a particular case of the previous equation.

Finite Differences Scheme

The approximation of derivatives by finite differences plays a central role in finite difference methods for the numerical solution of differential equations. If the spacing Δx is constant, using fourth-order Taylor expansion with $x_i = i\Delta x$, then a set of forward differences equations for A_{i+1}, A_{i+2} and A_{i+3} is as follows:

$$\begin{aligned}A_{i+1} &= A_i + A_x|_i\Delta x + \frac{1}{2}A_{xx}|_i\Delta x^2 \\ &\quad + \frac{1}{6}A_{xxx}|_i\Delta x^3 + O(\Delta x^4) \\ A_{i+2} &= A_i + 2A_x|_i\Delta x + \frac{4}{2}A_{xx}|_i\Delta x^2 \\ &\quad + \frac{8}{6}A_{xxx}|_i\Delta x^3 + O(\Delta x^4) \\ A_{i+3} &= A_i + 3A_x|_i\Delta x + \frac{9}{2}A_{xx}|_i\Delta x^2 \\ &\quad + \frac{27}{6}A_{xxx}|_i\Delta x^3 + O(\Delta x^4).\end{aligned}$$

The above equations can be written as a system of equations:

$$\begin{aligned}\frac{1}{6}A_{xxx}|_i\Delta x^3 + A_x|_i\Delta x + \frac{1}{2}A_{xx}|_i\Delta x^2 &= A_{i+1} - A_i + O(\Delta x^4) \\ \frac{8}{6}A_{xxx}|_i\Delta x^3 + 2A_x|_i\Delta x + \frac{4}{2}A_{xx}|_i\Delta x^2 &= A_{i+2} - A_i + O(\Delta x^4) \\ \frac{27}{6}A_{xxx}|_i\Delta x^3 + 3A_x|_i\Delta x + \frac{9}{2}A_{xx}|_i\Delta x^2 &= A_{i+3} - A_i + O(\Delta x^4).\end{aligned}$$

To solve the system, it can be written in matrix form:

$$\left[\begin{array}{ccc|c} 1/6 & 1 & 1/2 & A_{i+1} - A_i + O(\Delta x^4) \\ 8/6 & 2 & 4/2 & A_{i+2} - A_i + O(\Delta x^4) \\ 27/6 & 3 & 9/2 & A_{i+3} - A_i + O(\Delta x^4) \end{array}\right]$$

After adding and subtracting rows of the matrix, the system is:

$$\left[\begin{array}{ccc|c} 1/6 & 1 & 1/2 & A_{i+1} - A_i + O(\Delta x^4) \\ 0 & 6 & 4/2 & 8A_{i+1} - 7A_i - A_{i+2} + O(\Delta x^4) \\ 0 & 0 & -1 & 5A_{i+1} - 4A_{i+2} + A_{i+3} - 2A_i + O(\Delta x^4) \end{array}\right]$$

then the third row is the second-order Taylor expansion for forward differentiation at point i:

$$\begin{aligned}(\partial^2 A/\partial x^2)_i &= (2A_i - 5A_{i+1} + 4A_{i+2} - A_{i+3})/(\Delta x)^2 \\ &\quad + O(\Delta x^2)\end{aligned} \tag{67}$$

On the other hand, backward differences to A_{i-1}, A_{i-2}, and A_{i-3}, with $x - x_0 = (-\Delta x, -2\Delta x, -3\Delta x)$ in i, are respectively:

$$\begin{aligned}A_{i-1} &= A_i - A_x|_i\Delta x + \frac{1}{2}A_{xx}|_i\Delta x^2 \\ &\quad - \frac{1}{6}A_{xxx}|_i\Delta x^3 + O(\Delta x^4) \\ A_{i-2} &= A_i - 2A_x|_i\Delta x + \frac{4}{2}A_{xx}|_i\Delta x^2 \\ &\quad - \frac{8}{6}A_{xxx}|_i\Delta x^3 + O(\Delta x^4) \\ A_{i-3} &= A_i - 3A_x|_i\Delta x + \frac{9}{2}A_{xx}|_i\Delta x^2 \\ &\quad - \frac{27}{6}A_{xxx}|_i\Delta x^3 + O(\Delta x^4).\end{aligned}$$

Similarly to the previous case:

$$\left[\begin{array}{ccc|c} -1/6 & -1 & 1/2 & A_{i-1} - A_i + O(\Delta x^4) \\ -8/6 & -2 & 4/2 & A_{i-2} - A_i + O(\Delta x^4) \\ -27/6 & -3 & 9/2 & A_{i-3} - A_i + O(\Delta x^4) \end{array}\right]$$

$$\left[\begin{array}{ccc|c} -1/6 & -1 & 1/2 & A_{i-1} - A_i + O(\Delta x^4) \\ 0 & 6 & -4/2 & A_{i-2} - 8A_{i-1} + 7A_i + O(\Delta x^4) \\ 0 & 0 & -1 & A_{i-3} - 4A_{i-2} + 5A_{i-1} - 2A_i + O(\Delta x^4) \end{array}\right]$$

then the third row is the second-order Taylor expansion for backward differentiation at point i:

$$\begin{aligned}(\partial^2 A/\partial x^2)_i &= (2A_i - 5A_{i-1} + 4A_{i-2} - A_{i-3})/(\Delta x)^2 \\ &\quad + O(\Delta x^2).\end{aligned} \tag{68}$$

To obtain the central difference of second-order for A_x and A_{xx} at point i, we add and subtract the following equations:

$$\begin{aligned}A_{i+1} &= A_i + A_x|_i\Delta x + \frac{1}{2}A_{xx}|_i\Delta x^2 \\ &\quad + \frac{1}{6}A_{xxx}|_i\Delta x^3 + O(\Delta x^4) \\ A_{i-1} &= A_i - A_x|_i\Delta x + \frac{1}{2}A_{xx}|_i\Delta x^2 \\ &\quad - \frac{1}{6}A_{xxx}|_i\Delta x^3 + O(\Delta x^4)\end{aligned}$$

The results are:

$$(\partial A/\partial x)_i = (A_{i+1} - A_{i-1})/(2\Delta x) + O(\Delta x^2) \quad (69)$$

$$(\partial^2 A/\partial x^2)_i = (A_{i+1} - 2A_i + A_{i-1})/(\Delta x)^2 + O(\Delta x^2). \quad (70)$$

References

1. N. Al-Haddad, I.I. Roussev, C. Möstl, C. Jacobs, N. Lugaz, S. Poedts, C.J. Farrugia, On the internal structure of the magnetic field in magnetic clouds and interplanetary coronal mass ejections: writhe versus twist. Astrophys. J. Lett. **738**(2), L18 (2011)
2. J. Bittencourt, *Fundamentals of plasma physics*, 3rd edn, (2004). Originally published by Pergamon Press, New York, 1986, Verlag New York, Inc.
3. D. Du, C. Wang, Q. Hu, Propagation and evolution of a magnetic cloud from ACE to Ulysses. J. Geophys. Res. **112**(A9) (2007)
4. V. Fadeev, I. Kvabtskhava, N. Komarov, Self-focusing of local plasma currents. Nucl. Fusion **5**(202), 202–209 (1965)
5. J. Hadamard, *Lectures on Cauchy's problem in linear partial differential equations*, Dover Phoenix Editions (Dover Publications, 2003)
6. E.G. Harris, On a plasma sheath separating regions of oppositely directed magnetic field. Il Nuovo Cimento **23**(1), 115–121 (1962)
7. H. Hasegawa, R. Nakamura, M. Fujimoto, V.A. Sergeev, E.A. Lucek, H. Reme, Y. Khotyaintsev, Reconstruction of a bipolar magnetic signature in an earthward jet in the tail: flux rope or 3D guide-field reconnection? J. Geophys. Res. **112**(A11), A11206 (2007)
8. H. Hasegawa, B. Sonnerup, C. Owen, B. Klecker, G. Paschmann, A. Balogh, H. Reme, The structure of flux transfer events recovered from Cluster data. Ann. Geophys. **24**(2), 603–618 (2006)
9. H. Hasegawa, B.U.Ö. Sonnerup, B. Klecker, G. Paschmann, M.W. Dunlop, H. Reme, Optimal reconstruction of magnetopause structures from Cluster data. Ann. Geophys. **23**, 973–982 (2005)
10. L.-N. Hau, B.U.Ö. Sonnerup, Two-dimensional coherent structures in the magnetopause:recovery of static equilibria from single-spacecraft data. J. Geophys. Res. **104**(A4), 6899–6917 (1999)
11. P. Holoborodko, Smooth noise-robust differentiators. Tech. rep. http://www.holoborodko.com/pavel/?page (2008)
12. Q. Hu, C.W. Smith, N.F. Ness, R.M. Skoug, Multiple flux rope magnetic ejecta in the solar wind. J. Geophys. Res. Space **109**, 3102 (2004)
13. Q. Hu, B. Sonnerup, Reconstruction of magnetic clouds in the solar wind: orientations and configurations. J. Geophys. Res. **107**(A7), 1142, 15 (2002)
14. Q. Hu, B.U.Ö. Sonnerup, Magnetopause transects from two spacecraft: a comparison. Geophys. Res. Lett. **27**(10), 1443–1446 (2000)
15. Q. Hu, B.U.Ö. Sonnerup, Reconstruction of magnetic flux ropes in the solar wind. J. Geophys. Res. **28**(3), 467–470 (2001)
16. Q. Hu, B.U.Ö. Sonnerup, Reconstruction of two-dimensional structures in the magnetopause: method improvements. J. Geophys. Res. **108**(A1), 1011 (9 pp) (2003)
17. A. Isavnin, E. Kilpua, H. Koskinen, Grad-Shafranov reconstruction of magnetic clouds: overview and improvements. Sol. Phys. **273**(1), 205–219 (2011)
18. J. Kan, Non-linear tearing structures in equilibrium current sheet. Planet. Space. Sci. **27**(4), 351–354 (1979)
19. A.T.Y. Lui, Grad-Shafranov reconstruction of magnetic flux ropes in the near-Earth space. Space. Sci. Rev. **158**, 43–68 (2011)
20. A.T.Y. Lui, D.G. Sibeck, T. Phan, V. Angelopoulos, J. McFadden, C. Carlson, D. Larson, J. Bonnell, K.-H. Glassmeier, S. Frey, Reconstruction of a magnetic flux rope from THEMIS observations. Geophys. Res. Lett. **351**, 17 (2008)
21. C. Möstl, Modeling magnetic clouds using multi-spacecraft observations. Ph.D. thesis, Institut für Physik Institutsbereich Geophysik, Astrophysik und Meteorologie (2009)
22. A. Ojeda González, W.D. Gonzalez, O. Mendes, M.O. Domingues, R.R. Rosa, Nonlinear fluctuation analysis for a set of 41 magnetic clouds measured by the advanced composition explorer (ACE) spacecraft. Nonlinear Proc. Geoph. **21**(5), 1059–1073 (2014a)
23. A. Ojeda González, O. Mendes, M.A. Calzadilla, M.O. Domingues, Spatio-temporal entropy analysis of the magnetic field to help magnetic cloud characterization. J. Geophys. Res. Space **118**, 1–12 (2013)
24. A. Ojeda González, O. Mendes, M.O. Domingues, V.E. Menconi, Daubechies wavelet coefficients: a tool to study interplanetary magnetic fluctuations. Geofis. Int. **53**(1), 101–115 (2014b)
25. P. Riley, J. Linker, R. Lionello, Z. Mikic, D. Odstrcil, M. Hidalgo, C. Cid, Q. Hu, R. Lepping, B. Lynch, A. Rees, Fitting flux ropes to a global MHD solution: a comparison of techniques. J. Atmos. Sol.-Terr. Phy **66**(15–16), 1321–1331 (2004). towards an Integrated Model of the Space Weather System
26. B.U.Ö. Sonnerup, M. Guo, Magnetopause transects. Geophys. Res. Lett. **23**(25), 3679–3682 (1996)
27. B.U.Ö. Sonnerup, H. Hasegawa, G. Paschmann, Anatomy of a flux transfer event seen by Cluster. Geophys. Res. Lett. **31**, L11803–L11803 (2004)
28. B.U.Ö. Sonnerup, H. Hasegawa, W.-L. Teh, L.-N. Hau, Grad-Shafranov reconstruction: an overview. J. Geophys. Res. **111**(A09204), 1–12 (2006)
29. W.-L. Teh, A study of two-dimensional magnetopause structure based on Grad-Shafranov reconstruction method. Ph.D. thesis, Institute of Space Science, National Central University (2007)
30. W.-L. Teh, L.-N. Hau, Evidence for pearl-like magnetic island structures at dawn and dusk side magnetopause. Earth Planets Space **56**, L681 (2004)
31. W.-L. Teh, L.-N. Hau, Triple crossings of a string of magnetic islands at duskside magnetopause encountered by AMPTE/IRM satellite on 8 August 1985. J. Geophys. Res. **102**(A8), A08207 (2007)
32. G.W. Walker, Some problems illustrating the forms of nebulae. RSPSA **91**, 410–420 (1915)
33. P.H. Yoon, A.T.Y. Lui, A class of exact two-dimensional kinetic current sheet equilibria. J. Geophys. Res. **110**(A1), A01202 (2005)